RSC Advances

PAPER

View Article Online
View Journal | View Issue

Cite this: *RSC Adv.*, 2021, **11**, 462

Facile fabrication of Fe-doped Nb_2O_5 nanofibers by an electrospinning process and their application in photocatalysis†

Lu Wang, [ab] Ya Li, [c] Pingfang Han *[a] and Yunxia Jiang[c]

It is of top priority to develop highly efficient visible-light photocatalysts to realize the practical applications of photocatalysis in industry. Niobium pentoxide (Nb_2O_5) is considered as a potentially attractive candidate for the visible-light-driven photodegradation of organic pollutants. In an effort to enhance its photocatalytic activity, Fe-doped Nb_2O_5 nanofibers with various Fe contents (the molar ratios of Fe to Nb were 0.005/1, 0.01/1, 0.03/1 or 0.05/1) were successfully prepared by an electrospinning method. The structural features, morphologies, and optical properties of the as-prepared samples were investigated. Photocatalytic activities of the samples were evaluated through degradation of Rhodamine B (RhB) under visible light irradiation. All the prepared Fe-doped Nb_2O_5 nanofibers exhibited much higher activities for degrading RhB solution than the pristine Nb_2O_5 nanofibers, and the maximum degradation yield of 98.4% was achieved with the nanofibers (Fe to Nb: 0.03/1) under visible light irradiation for 150 min. The photocatalytic degradation rate fitted a pseudo-first-order equation, and the rate constants of reactions with Fe-doped Nb_2O_5 nanofiber (the molar ratios of Fe to Nb were 0.03/1) or pure Nb_2O_5 nanofiber were 0.0282 min^{-1} and 0.0019 min^{-1}, respectively. Doping Fe ions into the nanofibers enhanced the absorption within the visible-light range and reduced the photo-generated electron–hole pair recombination, and thus improved the photocatalytic activity. These attractive properties suggest that the Fe-doped Nb_2O_5 nanofibers have great potential for applications in the future to solve pollution issues.

Received 27th November 2020
Accepted 8th December 2020

DOI: 10.1039/d0ra10042k

rsc.li/rsc-advances

1. Introduction

Organic contamination in water is one of the major public concerns which is detrimental to human health and photocatalytic degradation of pollutants and toxins by semiconductor photocatalysts has attracted much attention due to the advantages of low cost, strong oxidizing activity, and high photosensitivity.[1,2] Among a variety of semiconductor photocatalysts, niobium pentoxide (Nb_2O_5) as an n-type photocatalyst displays a lot of unique physicochemical properties, including excellent chemical and thermal stability, and relatively high photocatalytic activity, making it a suitable photocatalyst for photodegradation.[3,4] However, Nb_2O_5 can only be activated under UV-light irradiation because of its large band gap of ~3.1 eV, making its use of solar energy less effective.[5,6] Additionally, the efficiency of a photocatalytic reaction is limited by a high recombination rate of photo-induced electron–hole pairs formed in the photocatalytic processes.[7,8] In this regard, many promising methods including metal and nonmetal doping, noble metal deposition or compositing with other semiconductor have been developed to improve the efficiency of Nb_2O_5 as a photocatalytic material.[9–15]

It has been proved that metal element doping was one of the most effective approaches to extend the spectral response of the wide-bandgap semiconductor to visible-light region.[16–18] Recently, some metal elements such as W, Mo, Fe, Cu and Mn have been employed to tune the electronic structure and enhanced the photocatalytic activity of the semiconductor photocatalysts.[19–27] For example, Esteves *et al.* found that W^{6+} or Mo^{6+} doping enhanced the photocatalytic activity of Nb_2O_5 towards methylene blue degradation due to the delay in the recombination time of excitons.[19] Ma *et al.* reported the highest Rhodamine B degradation efficiency under visible light irradiation for a WO_3 nanofiber sample containing 2% Cu^{2+} in their research results and the substitution of W^{6+} ions in the WO_3 lattice by Cu^{2+} ions was favored.[20] Baylan *et al.* used a electrospinning process to prepare Mn-doped ZnO nanofibers and studied the effect of Mn^{2+} and Mn^{4+} doping concentration on the photoactivity of methylene blue degradation.[21] Hu *et al.* studied the co-doping effect of N and Fe on nano-scaled TiO_2, which improved the activity under both visible and UV lights irradiation.[22] Among these elements, Fe^{3+} doping has attracted special attention. It was commonly believed that Fe^{3+} doping

[a]College of Biotechnology and Pharmaceutical Engineering, Nanjing Tech University, Nanjing 211816, China. E-mail: hpf@njtech.edu.cn
[b]Nantong Vocational University, Nantong 226007, China
[c]Nantong College of Science and Technology, Nantong 226007, China

† Electronic supplementary information (ESI) available. See DOI: 10.1039/d0ra10042k

was responsible for producing materials with intentional defects and lower band gap, diminishing the energy of the electron/hole pair formation and consequently increasing catalytic activity.[28–30]

It is well known that the crystal structure and morphology of semiconductors play significant roles in the photocatalytic activity because photogenerated charge separation and transfer are strongly affected by them.[31] Compared to bulk materials, nanomaterials exhibit a higher specific surface area, facilitating the interaction of a higher number of active sites with the pollutant molecules.[32] It has been reported that Nb_2O_5 with various morphologies like nanoparticle, nanorod, nanowire, nanofiber, nanosheet, nanobelt, nanonet and nanoflower demonstrated enhanced photocatalytic activities.[33–40] More attractively, Nb_2O_5 nanofibers are desirable material as a photocatalyst, because of its advantages of one-dimensional nanostructures, such as high surface-to-volume ratio, mechanical durability and reusability, and their porous structure providing the large number of surface active sites required for effective photocatalysis.[41] These unique features also provide flexibility in the surface modification of these materials.[42] Up to now, many researchers have fabricated Nb_2O_5 nanofibers using chemical deposition, solvothermal method, or electrospinning based methods.[43–48] Among these, electrospinning is an effective and versatile method which has been used for preparing organic and inorganic nanofibers with a variety of compositions and particle sizes.

A survey of the literature shows that Nb_2O_5 nanofibers are frequently investigated for their gas sensing or electrochemical properties, but little attention has been given towards their photocatalytic properties, particularly, there is no report on the electrospinning fabrication and photocatalysis performance of Fe-doped Nb_2O_5 nanofibers. Herein, we reported the preparation and investigation of a series of Fe-doped Nb_2O_5 nanofibers with homogeneous distribution of Fe ions. An electrospinning technique was utilized to synthesize the nanofibers, and their photocatalytic activity was then studied. A schematic representation of synthesis procedure of the Fe-doped Nb_2O_5 nanofibers is shown in Fig. 1. The obtained materials have been characterized by X-ray powder diffraction (XRD), Raman spectroscopy, scanning electron microscopy (SEM), transmission electron microscope (TEM), X-ray photoelectron spectroscopy (XPS), nitrogen adsorption for surface area, ultraviolet-visible diffuse reflectance spectra (UV-Vis DRS) and photoluminescence (PL) spectra. The photocatalytic activity of the obtained samples was investigated by the photodegradation of Rhodamine B (RhB) in aqueous solution at room temperature under visible light irradiation.

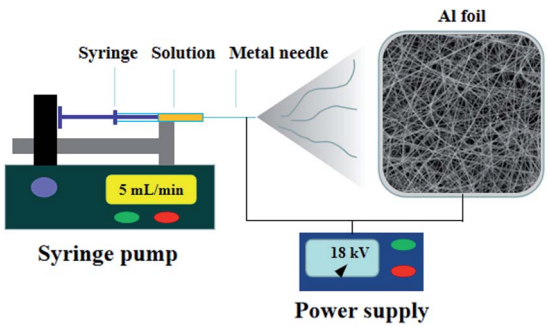

Fig. 1 Schematic diagram of the electrospinning setup used for the electrospun device.

2. Experimental methods

2.1 Samples preparation

In a typical procedure, 0.25 g of $NbCl_5$ and 1.25 mg of $FeCl_3 \cdot 6H_2O$ (molar ratio of Fe to Nb was 0.005/1) were dissolved in 2.65 mL of DMF, followed by the addition of 0.35 g of PVP. The mixture was then magnetically stirred for 6 h at room temperature. Electrospinning was conducted under the following conditions: flow rate at 5 mL min^{-1}, distance of 15 cm between the collector and the tip of needle (25 gauge), and an applied voltage of 18 kV. Subsequently, the Fe-doped Nb_2O_5 nanofibers were obtained by annealing the electrospun composite fibers at 600 °C in air for 1 h at a ramping rate of 10 °C min^{-1} and named as 0.005FeNb NFs. Similarly, the 0.01FeNb NFs, 0.03FeNb NFs and 0.05FeNb NFs samples (the molar ratios of Fe to Nb were 0.01/1, 0.03/1 and 0.05/1, respectively) were prepared. For comparison, pure Nb_2O_5 NFs was prepared under the same condition without adding $FeCl_3 \cdot 6H_2O$.

2.2 Characterization

Powder X-ray diffraction (XRD) data were acquired using a Rigaku ULTIMA IV diffractometer. Raman spectra of the

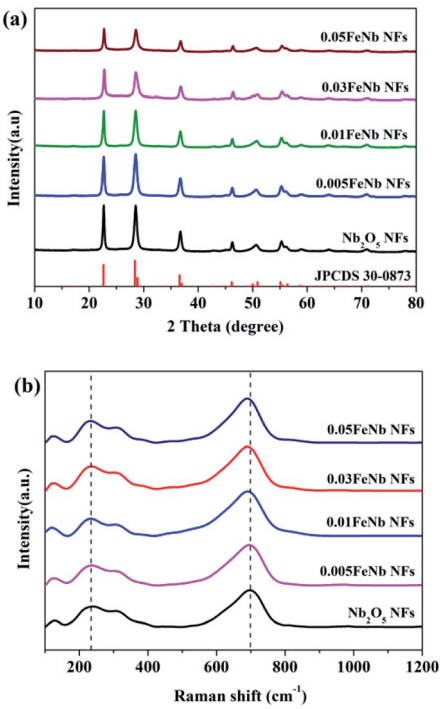

Fig. 2 (a) XRD patterns of pure Nb_2O_5 nanofibers, Fe-doped Nb_2O_5 nanofibers (0.005FeNb NFs, 0.01FeNb NFs, 0.03FeNb NFs and 0.05FeNb NFs) and standard XRD pattern of Nb_2O_5 (JCPDS 30-0873). (b) Raman spectra of pure Nb_2O_5 nanofibers and Fe-doped Nb_2O_5 nanofibers (0.005FeNb NFs, 0.01FeNb NFs, 0.03FeNb NFs and 0.05FeNb NFs).

samples were recorded on a Raman spectrometer of Bruker at a laser power of 16 mV with 256 scans. All spectra were recorded with the use of a 514.5 nm argon laser. The morphology and composition of samples were obtained by scanning electron microscopy (SEM, Hitachi SU8010) and transmission electron microscopy (TEM, JEM-2100F JEOL). The elemental compositions and electronic states of elements of the sample were analyzed by X-ray photoelectron spectroscopy (XPS, K-Alpha, Thermo Scientific). The textural properties of the materials were analyzed by a nitrogen adsorption analyzer apparatus (Micromeritics ASAP 2460). The ultraviolet-visible diffuse reflectance spectra (UV-Vis DRS) of samples were recorded on a Shimadzu UV-2600 spectrophotometer. Photoluminescence (PL) spectra were recorded using a Hitachi F-4600 spectrophotometer.

2.3 Photocatalytic activity experiment

The photocatalytic performances of all catalysts for the degradation of RhB were evaluated under visible light (300 W xenon lamp, $\lambda > 420$ nm). The temperature of the reaction system was kept at 25 ± 2 °C by cycling water. Typically, 0.1 g of catalyst was added into 100 mL of RhB (10 mg L^{-1}) solution. The suspension was magnetically stirred for 30 min before the light irradiation. During the irradiation, approximately 2 mL of solution was sampled at defined time intervals and centrifuged. The RhB concentration in the solution was analyzed by the absorption at 554 nm using a UV-1801 spectrophotometer. The degradation rate of the RhB solution was calculated using the following equation:

$$\eta = [(C_0 - C_t)/C_0] \times 100\% \quad (1)$$

where η is the decomposition efficiency, C_0 is the initial concentration of the RhB and C_t is the concentration of the RhB at the given reaction time [t (min)].

3. Results and discussion

3.1 Structure and morphology

The crystalline structures of pure Nb_2O_5 NFs and Fe-doped Nb_2O_5 NFs were characterized by XRD (Fig. 2a). The diffraction peaks of the prepared samples at 22.6°, 28.4°, 28.9°, 36.6°, 46.1°, 50.0°, 50.9°, 55.4°, 56.4° and 58.8° can be indexed to the (001), (180), (200), (181), (002), (0160), (380), (202), (381) and (2160) planes of orthorhombic Nb_2O_5 (JPCDS no. 30-0873), respectively.[49] With the increasing Fe contents, no apparent peaks of iron oxides or other phases could be detected in the doped products, suggesting that the existence of Fe in the product hardly affect the crystallization properties of niobium oxide. This could be attributed to the fact that the Fe concentrations were low and the radius of Fe^{3+} (0.645 Å) and the radius of Nb^{5+} (0.64 Å) are nearly equal. Thus, the Fe^{3+} ions could dope into the crystal lattice of Nb_2O_5, forming an iron–niobium finite solid solution.

To further obtain more structural and bonding environment information about the Fe-doped Nb_2O_5 nanofibers, the Raman spectra of all samples were collected. As shown in Fig. 2b, pure Nb_2O_5 only contained the characteristic peaks of the orthorhombic phase. A main vibration mode at ~700 cm^{-1} is related to the vibration of weakly distorted NbO_6 octahedral. The peaks in the range of 420–780 cm^{-1} are assigned to the symmetrical stretching of the Nb_2O_5 polyhedron, and other peaks between 200 and 360 cm^{-1} are attributed to the angular deformation modes of the Nb–O–Nb bonds.[50] Upon Fe doping, no other peaks corresponding to the modes of the Fe–O bonds in all products was observed, consistent with the results of XRD. Remarkably, the characteristic peaks of the products were gradually broadened and shifted to lower wavenumbers with the increase of iron contents, which may be resulted from iron occupying the substitutional site in Nb_2O_5.[29]

The morphology of the Fe-doped Nb_2O_5 nanofibers (taking the case of 0.03FeNb NFs) was investigated by SEM and TEM. Fig. S1a† displays the precursor of 0.03FeNb NFs, which has 1D nanofibers morphology with random orientation and more than 100 μm in length. Fig. S1b and c† represent the precursor nanofibers with an average diameter of 200 nm and have a uniform and smooth surface, because of amorphous polymeric nature of PVP–niobium chloride composite fibers. A corresponding SEM image after the 600 °C heat treatment in air of the composite sample is shown in Fig. S1d,† clearly indicating the resultant products replicate the initial profile with the similar nanofiber morphology. However, compared with the precursor, the images with higher magnification shown in Fig. 3a and b reveal that the sample 0.03FeNb NFs has an obviously rougher surface morphology, which consist of nanocrystals with an average size of 20–50 nm. The formation of this morphology was due to the shrinkage caused by degradation of PVP, decomposition of niobium source, and subsequent locating along the 1D direction during the calcination process.

Fig. 3c presents a typical TEM image of the obtained sample 0.03FeNb NFs, revealing the well-defined 1D nanofiber morphology. Typical TEM mapping pictures and the corresponding EDX pattern of 0.03FeNb NFs identify the Fe impurity atoms in Nb_2O_5 nanofibers. As shown in Fig. 3d–f, the elements Nb, O and Fe are all distributed uniformly in the composite nanofiber. The corresponding EDX result (Fig. 3g) clearly showed the peak of Fe in the composite and the content of Fe in the nanofiber was 1.83 wt%. No impurities were observed in the samples. Additionally, a HRTEM image of 0.03FeNb NFs (Fig. 3h) reveals the lattice fringes with d-spacing of 0.242 nm, in agreement with the (201) interplanar distance of the orthorhombic structure of Nb_2O_5.[45]

To quantitatively examine the surface area and porosity of 0.03FeNb NFs, Brunauer–Emmett–Teller (BET) and Barrett–Joyner–Halenda (BJH) analysis were further conducted (Fig. S2a†). N_2 adsorption–desorption isotherm graph demonstrates a high adsorption at a relative pressure (P/P_0) higher than 0.7, which suggests that many mesopores were extant on 0.03FeNb NFs. The specific surface areas of 0.03FeNb NFs were calculated to be 24.5 $m^2\ g^{-1}$. The pore size distribution of 0.03FeNb NFs (Fig. S2b†) indicates that mesopores are predominantly present in 0.03FeNb NFs, where the pore volume is highly concentrated in the pore diameter in the

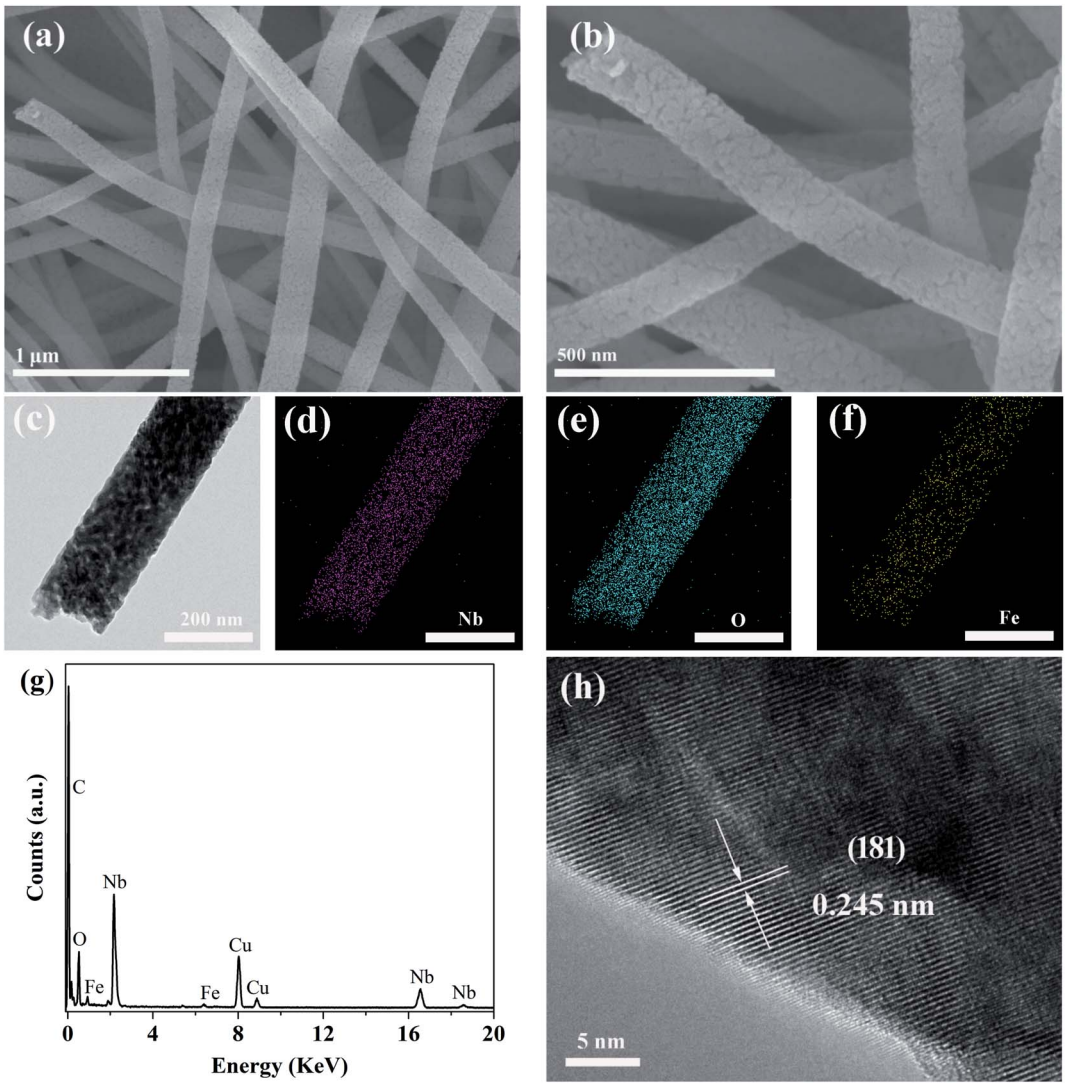

Fig. 3 (a and b) SEM images of 0.03FeNb NFs. (c) TEM image of 0.03FeNb NFs. (d–f) The corresponding TEM mapping analysis of Nb, O and Fe. (g) The corresponding EDX analysis of (c). (h) High-magnified TEM image of (c).

range of 5–30 nm. Such mesoporous structure is favorable for catalysis.[51]

Fig. 4a presented the overview of XPS spectrum of 0.03FeNb NFs. Elements of C, Nb, O and Fe were observed and their corresponding photoelectron peaks were C 1s, Nb 3d, O 1s and Fe 2p, respectively. The carbon peak was attributed to adventitious hydrocarbon from XPS instrument itself. The Nb 3d spectra were shown in Fig. S3a.† Pure Nb_2O_5 NFs presented two strong peaks located at 207.4 and 210.1 eV, corresponding to $3d_{5/2}$ and $3d_{3/2}$ states of Nb(v), respectively. These data agreed well with previously reported data.[52] Notably, for the 0.01FeNb NFs and 0.03FeNb NFs sample, the Nb $3d_{5/2}$ peak shifted to 207.2 eV and 206.9 eV, respectively. These shifts were ascribed to the interaction of the Nb species with dopant. The larger the Fe^{3+} contents, the more the binding energy of Nb decreases.[13] The high resolution XPS spectrum of the Fe 2p was shown in Fig. 4b. The peak of the Fe 2p at 711.2 eV could be attributed to $2p_{3/2}$ of Fe^{3+} ions.[53] This peak value was distinct from that of Fe^{3+} in Fe_2O_3 (at 710.7 eV).[54] The Fe element in the samples exists mainly in the +3 oxidation state (Fe^{3+}). Since the radiuses of Fe^{3+} and Nb^{5+} are similar, the Fe^{3+} could be incorporated into the lattice of Nb_2O_5 to form Nb–O–Fe bonds in the Fe–Nb_2O_5 microsphere by calcination at 600 °C in air. Fig. S3b† depicted the O 1s core level binding of the doped samples. The O 1s XPS spectrum could be fitted into distinct components, demonstrating that different kinds of O binding states were existed in Fe-doped Nb_2O_5 nanofibers. The predominant peak was assigned to the crystal lattice oxygen (Fe–O and Nb–O).

The UV-Vis diffuse reflectance spectra of the samples were shown in Fig. 5. These products exhibited absorption in both UV and visible-light regions. Obviously, the diffuse reflectance spectra of all Fe-doped Nb_2O_5 NFs displayed a red shift and increased absorption in the visible-light range. The higher iron content, the greater degree of red shift. The bandgap of the samples calculated from the Tauc plots (Fig. S4†) using Kubelka–Munk theory was listed in Table 1. As shown, with the

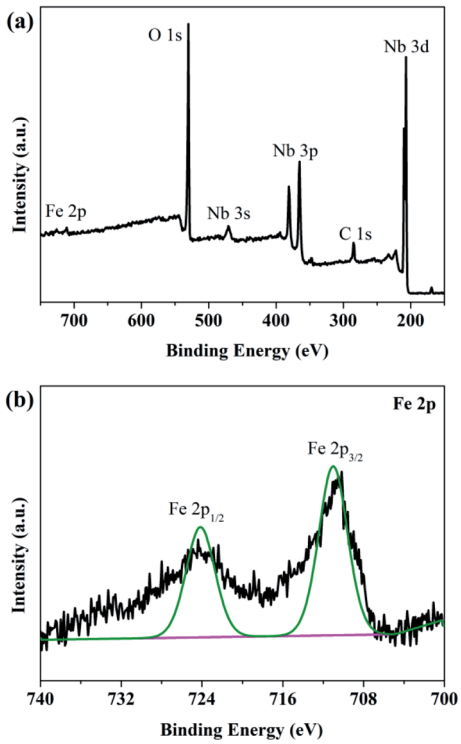

Fig. 4 (a) Overview XPS spectrum and (b) XPS spectra of the Fe 2p region of 0.03FeNb NFs.

increasing of Fe contents, the band gap of the samples decreased gradually. This was due to the fact that the doping Fe ions could create a donor level above the original valence band of Nb_2O_5 to narrow the band gap.[23] Thus, these results demonstrated that the Fe ions were indeed incorporated into the lattice of Nb_2O_5.

3.2 Photocatalytic performance

The photocatalytic performances of Fe-doped Nb_2O_5 nanofibers were assessed by degrading RhB under visible light ($\lambda >$ 420 nm). Fig. 6a presents the RhB degradation results with

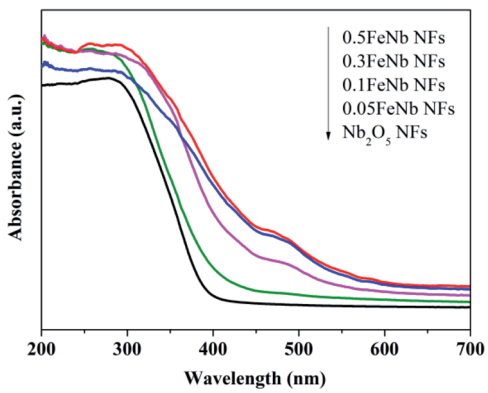

Fig. 5 UV-Vis DRS of pure Nb_2O_5 nanofibers and Fe-doped Nb_2O_5 nanofibers (0.005FeNb NFs, 0.01FeNb NFs, 0.02FeNb NFs, 0.03FeNb NFs and 0.05FeNb NFs).

Table 1 Bandgap values for pure Nb_2O_5 nanofibers and Fe-doped Nb_2O_5 nanofibers (0.005FeNb NFs, 0.01FeNb NFs, 0.02FeNb NFs, 0.03FeNb NFs and 0.05FeNb NFs)

Nanofibers	Bandgap [eV]
0.05FeNb	2.65
0.03FeNb	2.82
0.01FeNb	2.95
0.005FeNb	3.27
Pure Nb_2O_5	3.38

different catalyst. All the Fe-doped Nb_2O_5 nanofibers exhibit higher photocatalytic activity than pure Nb_2O_5 nanofibers, suggesting that doping Fe^{3+} in the Nb_2O_5 nanofibers is an effective route to enhance the photocatalytic activity of Nb_2O_5 nanofibers. With the increase of Fe ions contents, the RhB degradation performance of different Fe-doped Nb_2O_5 nanofibers increases first and then decreases with doping concentration. Compared with other samples, 0.03FeNb NFs presented the maximum degradation percentage 98.4% under visible-light irradiation for 150 min. Fig. 6b shows the UV-Vis spectra of the RhB aqueous solution with the reaction time in the presence of 0.03FeNb NFs. A decrease in intensity of the absorption peak of RhB (major peak at 552 nm) can be observed with prolong the reaction time to about 150 min, which indicates that the RhB molecules are gradually

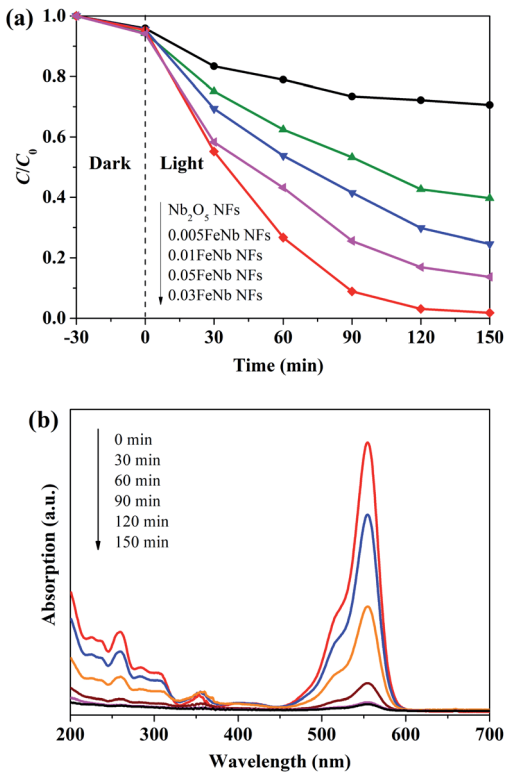

Fig. 6 (a) Photocatalytic degradation of RhB with various catalysts under visible light. (b) Absorption spectra of RhB with irradiation time in the presence of 0.03FeNb NFs.

Table 2 Reaction rate constant and R^2 values for the photocatalytic degradation of RhB in visible light

Nanofibers	k/min^{-1}	R^2
0.05FeNb	0.0132	0.98321
0.03FeNb	0.0282	0.86302
0.01FeNb	0.0091	0.99564
0.005FeNb	0.0059	0.98422
Pure Nb_2O_5	0.0019	0.98697

degraded. The reaction kinetics of RhB degradation over various catalysts was further studied. The experimental data could be fitted well with the pseudo-first-order model (Fig. S5†). The calculated rate constants were listed in Table 2. It was found that 0.03FeNb NFs had the highest rate constant value of 0.0282 min^{-1}, which was approximately 14.8 times higher than pure Nb_2O_5 nanofibers (k = 0.0019 min^{-1}).

3.3 Degradation mechanism

Under visible light irradiation, the pure Nb_2O_5 nanofibers were excited and generated electron–hole pairs are recombined much easier. However, when Fe^{3+} ions were introduced, Nb_2O_5 nanofibers composites were easily excited by visible light. Meanwhile, Fe^{3+} ions could trap and transfer electrons and holes to inhibit the recombination of photo-excited holes and electrons, which trigger the degradation reactions.[53] According to literature, the proposed photocatalytic mechanism for the Fe-doped Nb_2O_5 nanofibers photocatalyst can be schematically shown in Fig. 7a.[29]

To confirm the above effective charge separation mechanism in the Fe-doped Nb_2O_5 nanofibers, quenching experiments were performed using *tert*-butyl alcohol (BuOH) as ·OH scavenger, and ethylenediaminetetraacetic acid disodium salt (EDTA) as hole scavenger. Fig. 7b showed the degradation rate of RhB under different condition using 0.03FeNb NFs as the photocatalyst. It was found that 98% of RhB was degraded under visible light irradiation within 150 min. However, in the presence of BuOH or EDTA, the degradation rate was reduced to 28% or 41% under otherwise identical condition, respectively. So, the photocatalytic degradation of RhB was mainly

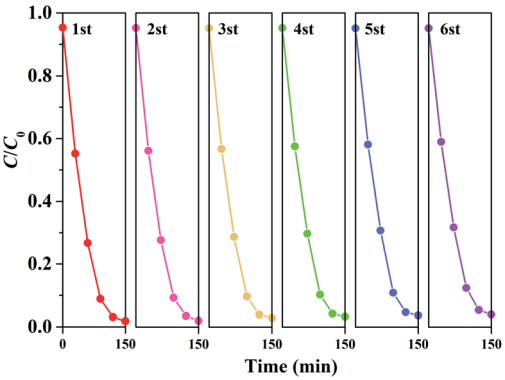

Fig. 8 The reusability of 0.03FeNb NFs photocatalyst.

caused by ·OH radicals, which were mostly produced by Fe^{3+} and hole. Therefore, we can conclude that Fe^{3+} ions were beneficial to the separation of electron–hole pairs. However, when the amount of Fe^{3+} ions goes higher, more Fe^{3+} ions were accumulated in the interior of the nanofibers. Fe^{3+} ions usually act as recombination centers for the photo-excited electrons and holes, resulting in the decreasing of the photocatalytic performance.[55]

The PL spectrum was used to investigate the charge recombination and transfer behavior. The PL spectra of pure Nb_2O_5 NFs and 0.03FeNb NFs with an excitation wavelength at 325 nm, are given in Fig. 7c. Both of nanofibers show a prominent emission band centered at about 480 nm, which corresponds to the recombination of electron–hole pairs. In addition, we can clearly see that the pure Nb_2O_5 NFs show higher intensity than 0.03FeNb NFs, which suggests that the pure Nb_2O_5 NFs has higher recombination rate of electron–hole pair than that of 0.03FeNb NFs. The PL results illustrate that the doping of Fe ions could suppress the electron–hole recombination, thereby increasing the visible light photocatalytic activity of Nb_2O_5.

Fig. 8 displays the RhB photodegradation performance in a cycling sequence of photocatalytic runs. After six cycles, the degradation rate of RhB over 0.03FeNb NFs remained above 94%, illustrating the excellent stability of 0.03FeNb NFs.

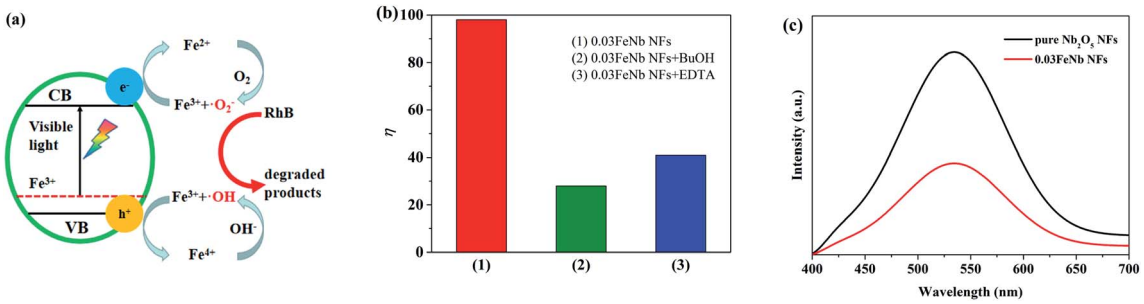

Fig. 7 (a) A schematic diagram of the charge separation and the photocatalytic activity for the Fe-doped Nb_2O_5 nanofibers photocatalyst. (b) Radical-scavenge tests in the removal of RhB in the presence of 0.03FeNb NFs. (c) PL spectra of pure Nb_2O_5 NFs and 0.03FeNb NFs with an excitation wavelength of 325 nm.

4. Conclusions

We reported the fabrication and photocatalytic investigation of Fe doped Nb_2O_5 nanofibers under visible light irradiation. It was found that photocatalytic activity of the Nb_2O_5 under visible light was improved significantly by the doping of Fe. The absorption edge of the Nb_2O_5 shifted from UV region to the visible light, with the doping of Fe. In addition, Fe dopant retarded the electron/hole pairs recombination process. Fe incorporation in the Nb_2O_5 first increased the photocatalytic efficiency and then decreased it as the Fe amount was increased. The best Fe to Nb ratio was determined to be 0.03/1 in a model reaction of photo decomposition of RhB, and a degradation yield of 98.4% was achieved. This research provides a general and effective method to synthesize different photocatalysts with enhanced visible-light-driven photocatalytic performance, and should be of great interest for a large range of applications.

Conflicts of interest

There are no conflicts to declare.

Acknowledgements

This work was financially supported by the Natural Science Foundation of the Jiangsu Higher Education Institutions of China (No. 18KJB610016), the Qing Lan Project of Jiangsu Province, the Science and Technology Program of Nantong (No. JC2019160 and No. JC2018080).

Notes and references

1 S. Zhu and D. Wang, *Adv. Energy Mater.*, 2017, **7**, 1700841.
2 S. Li, S. Hu, K. Xu, W. Jiang, J. Liu and Z. Wang, *Nanomaterials*, 2017, **7**, 22–34.
3 H. Huang, J. Zhou, J. Zhou and M. Zhu, *Catal. Sci. Technol.*, 2019, **9**, 3373–3379.
4 H. Huang, C. Wang, J. Huang, X. Wang, Y. Du and P. Yang, *Nanoscale*, 2014, **6**, 7274–7280.
5 J. Xue, R. Wang, Z. Zhang and S. Qiu, *Dalton Trans.*, 2016, **45**, 16519–16525.
6 S. G. Ghugal, S. S. Umare and R. Sasikala, *RSC Adv.*, 2016, **6**, 64047–64055.
7 J. Bai, J. Xue, R. Wang, Z. Zhang and S. Qiu, *Dalton Trans.*, 2018, **47**, 3400–3407.
8 J. Wu, J. Li, J. Liu, J. Bai and L. Yang, *RSC Adv.*, 2017, **7**, 51046–51054.
9 A. K. Kulkarni, C. S. Praveen, Y. A. Sethi, R. P. Panmand, S. S. Arbuj, S. D. Naik, A. V. Ghule and B. B. Kale, *Dalton Trans.*, 2017, **46**, 14859–14865.
10 X. Wang, G. Chen, C. Zhou, Y. Yu and G. Wang, *Eur. J. Inorg. Chem.*, 2012, 1742–1749.
11 T. Xie, H. Zhao, Z. Lv, G. Xie and Y. He, *Int. J. Hydrogen Energy*, 2020, DOI: 10.1016/j.ijhydene.2020.09.244.
12 B. Boruah, R. Gupta, J. M. Modak and G. Madras, *Nanoscale Adv.*, 2019, **1**, 2748–2760.
13 H. Zhang, Q. Lin, S. Ning, Y. Zhou, H. Lin, J. Long, Z. Zhang and X. Wang, *RSC Adv.*, 2016, **6**, 96809–96815.
14 Y. Wang, X. Kong, M. Jiang, F. Zhang and X. Lei, *Inorg. Chem. Front.*, 2020, **7**, 437–446.
15 R. G. Marques, A. M. Ferrari-Lima, V. Slusarski-Santana and N. R. C. Fernandes-Machado, *J. Environ. Manage.*, 2017, **195**, 242–248.
16 M. Wu, P. Wu, T. Lin and T. Lin, *Appl. Surf. Sci.*, 2018, **430**, 390–398.
17 Y. Tian, L. Cheng and J. Zhang, *J. Electrochem. Soc.*, 2018, **165**, 284–290.
18 H. Lin, H. Yang and W. Wang, *Catal. Today*, 2011, **174**, 106–113.
19 A. Esteves, L. C. A. Oliveira, T. C. Ramalho, M. Goncalves, A. S. Anastacio and H. W. P. Carvalho, *Catal. Commun.*, 2008, **10**, 330–332.
20 G. Ma, J. Lu, Q. Meng, H. Lv, L. Shui, Y. Zhang, M. Jin, Z. Chen, M. Yuan, R. Nötzel, X. Wang, C. Wang, J. Liu and G. Zhou, *Appl. Surf. Sci.*, 2018, **451**, 306–314.
21 E. Baylan and O. Z. Yildirim, *Mater. Sci. Semicond. Process.*, 2019, **103**, 104621.
22 S. Hu, F. Li, Z. Fan and C. Chang, *Appl. Surf. Sci.*, 2011, **258**, 182–188.
23 H. Moradi, A. Eshaghi, S. R. Hosseini and K. Ghani, *Ultrason. Sonochem.*, 2016, **32**, 314–319.
24 J. Chen, Y. Xiong, M. Duan, X. Li, J. Li, S. Fang, S. Qin and R. Zhang, *Langmuir*, 2020, **36**, 520–533.
25 H. Nishikiori, T. Sato, S. Kubota, N. Tanaka, Y. Shimizu and T. Fujii, *Res. Chem. Intermed.*, 2012, **38**, 595–613.
26 M. Lu, Q. Li, C. Zhang, X. Fan and H. Shi, *Int. J. Mod. Phys. B*, 2019, **33**, 1950270.
27 M. Gharagozlou and R. Bayati, *Mater. Res. Bull.*, 2015, **61**, 340–347.
28 K. Kumar, M. Chitkara, I. S. Sandhu, D. Mehta and S. Kumar, *J. Alloys Compd.*, 2014, **588**, 681–689.
29 H. Song, Y. Li, Z. Lou, M. Xiao, L. Hu, Z. Ye and L. Zhu, *Appl. Catal., B*, 2015, **166–167**, 112–120.
30 J. Yu, Q. Xiang and M. Zhou, *Appl. Catal., B*, 2009, **90**, 595–602.
31 Y. Liu, P. Fang, Y. Cheng, Y. Gao, F. Chen, Z. Liu and Y. Dai, *Chem. Eng. J.*, 2013, **219**, 478–485.
32 Z. Zeng, Y. Xu, Z. Zhang, Z. Gao, M. Luo, Z. Yin, C. Zhang, J. Xu, B. Huang, F. Luo, Y. Du and C. Yan, *Chem. Soc. Rev.*, 2020, **49**, 1109–1143.
33 O. F. Lopes, E. C. Paris and C. Ribeiro, *Appl. Catal., B*, 2014, **144**, 800–808.
34 W. Zhao, W. Zhao, G. Zhu, T. Lin, F. Xu and F. Huang, *Dalton Trans.*, 2016, **45**, 3888–3894.
35 K. Saito and A. Kudo, *Bull. Chem. Soc. Jpn.*, 2009, **82**, 1030–1034.
36 S. Qi, L. Fei, R. Zuo, Y. Wang and Y. Wu, *J. Mater. Chem. A*, 2014, **2**, 8190–8195.
37 X. Liu, W. Que, Y. Xing, Y. Yang, X. Yin and J. Shao, *RSC Adv.*, 2016, **6**, 9581–9588.
38 B. Hu and Y. Liu, *J. Alloys Compd.*, 2015, **635**, 1–4.
39 F. A. Qaraah, S. A. Mahyoub, M. E. Hafez and G. Xiu, *RSC Adv.*, 2019, **9**, 39561–39571.

40 F. Idrees, C. Cao, R. Ahmed, F. K. Butt, S. Butt, M. Tahir, M. Tanveer, I. Aslam and Z. Ali, *Sci. Adv. Mater.*, 2015, **7**, 1298.
41 S. Qi, R. Zuo, Y. Liu and Y. Wang, *Mater. Res. Bull.*, 2013, **48**, 1213–1217.
42 R. Shao, X. Zeng, Z. Cao, H. Dong, L. Wang, F. Wang, J. Liu, Z. Li and Q. Liang, *RSC Adv.*, 2015, **5**, 102101–102107.
43 K. Saito and A. Kudo, *Dalton Trans.*, 2013, **42**, 6867–6872.
44 Y. Zhang, H. Zhao, X. Zhao, J. Lin, N. Li, Z. Huo, Z. Yan, M. Zhang and S. Hu, *Sci. China Mater.*, 2019, **62**, 203–210.
45 J. Cheong, J. Jung, D. Youn, C. Kim, S. Yu, S. Cho, K. Yoon and I. Kim, *J. Power Sources*, 2017, **360**, 434–442.
46 A. L. Viet, M. V. Reddy, R. Jose, B. V. R. Chowdari and S. Ramakrishna, *J. Phys. Chem. C*, 2010, **114**, 664–671.
47 L. Lou, X. Kong, T. Zhu, J. Lin, S. Liang, F. Liu, G. Cao and A. Pan, *Sci. China Mater.*, 2019, **62**, 465–473.
48 G. C. Leindecker, A. K. Alves and C. P. Bergmann, *Ceram. Int.*, 2014, **40**, 16195–16200.
49 J. Zhai, Y. Wu, X. Zhao and Q. Yang, *J. Alloys Compd.*, 2017, **715**, 275–283.
50 H. Zhang, Q. Wu, C. Guo, Y. Wu and T. Wu, *ACS Sustainable Chem. Eng.*, 2017, **5**, 3517–3523.
51 X. Li, J. G. Yu and M. Jaroniec, *Chem. Soc. Rev.*, 2016, **45**, 2603–2636.
52 Z. Dai, H. Dai, Y. Zhou, D. Liu, G. Duan, W. Cai and Y. Li, *Adv. Mater. Interfaces*, 2015, **2**, 1500167.
53 T. Tong, J. Zhang, B. Tian, F. Chen and D. He, *J. Hazard. Mater.*, 2008, **155**, 572–579.
54 T. Yamashita and P. Hayes, *Appl. Surf. Sci.*, 2008, **254**, 2441–2449.
55 R. Dholam, N. Patel, M. Adami and A. Miotello, *Int. J. Hydrogen Energy*, 2009, **34**, 5337–5346.